Journal of Sound and Vibration 642 (2026) 119960

Contents lists available at ScienceDirect

Journal of Sound and Vibration

journal homepage: www.elsevier.com/locate/jsvi

Extended Gao beam under moving inertial load

Bartłomiej Dyniewicz [a,*], Czesław I. Bajer [a,*], Jitka Machalová [b], Horymír Netuka [b]

[a] Institute of Fundamental Technological Research, Polish Academy of Sciences, Pawińskiego 5b, 02-106 Warsaw, Poland
[b] Department of Mathematical Analysis and Applications of Mathematics, Faculty of Science, Palacký University, 17. Listopadu 12, 779 00, Olomouc, Czech Republic

ARTICLE INFO

Keywords:
Structural dynamics
Extended Gao beam
Moving mass
Inertial load
Non-linear dynamics
Shear deformation

ABSTRACT

This paper investigates the dynamic behaviour of a thick Gao beam subjected to high-velocity inertial moving loads and substantial axial compressive forces. This approach addresses a significant gap by combining geometric nonlinearity, transverse shear deformation, and complete inertial effects (including Coriolis and centrifugal forces). The mathematical model consists of two strongly coupled nonlinear hyperbolic partial differential equations, solved using the finite element method with space-time integration. Key findings include: (1) nonlinearity produces substantial geometric stiffening effects, with deflections decreasing by factors of 2-3 compared to linear models; (2) supercritical axial compression induces snap-through phenomena and bifurcation between equilibrium states; (3) under combined compression and moving loads, beam deflections are primarily governed by axial force magnitude rather than load weight, with multiple passages producing non-repeating response patterns; (4) maximum accelerations occur neither at mid-span nor at support entry, remaining relatively insensitive to transit velocity. The results indicate a strong detuning between the beam oscillations and the load transition cycles, especially at higher velocities. These findings have important implications for railway bridge design and structures experiencing simultaneous thermal stresses and dynamic vehicular loads, where simplified linear models may significantly underestimate dynamic effects.

1. Introduction

This paper continues the investigation of the dynamics of structural systems subjected to inertial moving loads. Particular attention is devoted to situations in which the velocity of the moving load is comparable to the propagation speed of waves in real structures.

In railway systems, bending waves in rails propagate at velocities ranging from several hundred to several thousand meters per second. Waves in ballast and soil (Rayleigh waves) propagate at about 100–300 m/s in soft soils and 500–800 m/s in rocky soils, while in water-saturated soils the shear-wave velocity may decrease to as little as 50 m/s. By contrast, bending waves in bridge or viaduct spans typically propagate at velocities between 50 and 500 m/s, and for structures resting on saturated soils, the velocities may be even lower. These relatively slow waves are responsible for noticeable and often harmful paraseismic vibrations in the vicinity of railway lines.

* Corresponding authors.
E-mail addresses: bdynie@ippt.pan.pl (B. Dyniewicz), cbajer@ippt.pan.pl (C.I. Bajer), jitka.machalova@upol.cz (J. Machalová), horymir.netuka@upol.cz (H. Netuka).

https://doi.org/10.1016/j.jsv.2026.119960
Received 16 January 2026; Received in revised form 15 May 2026; Accepted 13 June 2026
Available online 16 June 2026

The dynamics of structures subjected to moving loads has been studied for many decades in structural mechanics and civil engineering. Classical models usually represent the travelling load as a prescribed force moving along the structure without accounting for the inertia of the load itself. Such formulations lead to relatively simple mathematical problems for which analytical solutions can often be obtained, typically in the form of Fourier series expansions. A comprehensive overview of this class of problems can be found in the monograph [1], and the non-inertial moving-load problem is generally regarded as well understood from the analytical perspective.

The situation changes significantly when the inertia of the travelling load is taken into account. In this case, the load is modelled as a moving mass, which introduces coefficients depending simultaneously on time and spatial position in the governing equations. As a consequence, exact analytical solutions for the general formulation of the problem are not available, and most studies rely on approximate or numerical approaches.

The moving mass problem has been studied most extensively for Bernoulli-Euler beams. In [2], the dynamic response of a beam subjected to a moving mass was compared with the response obtained for a moving force, demonstrating that the inertia of the load may lead to significantly larger vibration amplitudes and dynamic effects not captured by simplified models. Hybrid and semi-analytical solution strategies were proposed in [3], while [4] addressed discontinuities in internal force distributions generated by moving masses. Parametric investigations reported in [5] showed that the Bernoulli-Euler theory may become inadequate for beams with small slenderness ratios or at high travelling velocities.

A more refined structural description can be obtained using the Timoshenko beam theory, which accounts for shear deformation and rotary inertia. Dynamic responses of such beams under moving loads were investigated using discrete element and finite element approaches in [6,7]. These studies demonstrated that shear effects and beam thickness may significantly influence the dynamic response. More recent investigations have incorporated advanced material and foundation models. For example, in [8], a nonlinear Timoshenko beam resting on a fractional Pasternak foundation was analysed, showing that fractional operators can accurately capture structural responses under moving loads. Comparisons between Bernoulli-Euler and Timoshenko beams subjected to inertial moving loads reveal important qualitative differences [9,10]. In particular, the Timoshenko model predicts large reaction forces at the end support when the moving mass leaves the span [11], a phenomenon absent in the Bernoulli-Euler formulation but frequently observed in real structures such as rail joints or pavement edges.

The moving mass problem has also been investigated for other continuous systems. Methods based on complex eigenfunctions were proposed for strings in [12], where discontinuities in the trajectory of a moving mass near the support were identified [11]. Extensions to two-dimensional structures include plates subjected to moving masses. Finite element formulations incorporating complete inertial effects were developed in [13], while space–time finite element approaches for Mindlin plates were presented in [14]. These studies showed that inertial effects become particularly significant at high velocities and may strongly modify structural response. Similar formulations have also been proposed for spatial structures in which the motion of the particle and the deformable structure are fully coupled [15].

In recent years, increasing attention has been devoted to moving-mass problems in nonlinear structural models. One example is the nonlinear Gao beam, which accounts for large deformations and axial interactions. Studies reported in [16] demonstrated substantial differences between the dynamic responses of the Gao beam and the classical Bernoulli-Euler beam. The mathematical existence of solutions for a Gao beam subjected to a moving mass was established in [17]. The Gao beam model itself has been extensively studied with respect to its mathematical properties, vibrations, crack propagation, and interactions with foundations or constraints [18–22]. Recent works also address parameter identification [23,24] and buckling or post-buckling states involving multiple equilibrium configurations [25].

Despite these extensive studies, most analyses of inertial moving loads employ simplified beam models, whereas investigations of the Gao beam rarely include moving loads. Consequently, the combined influence of inertial moving loads, shear deformation, and axial effects in thick Gao-type beams remains insufficiently explored.

The present work aims to investigate the dynamic behaviour of a thick Gao-type beam subjected to a high-velocity inertial moving load while simultaneously accounting for axial forces. Such forces may arise, for example, from temperature variations in railway rails, where temperature changes exceeding 60 °C within a single day and 80 °C over a year may generate significant axial stresses. These stresses can substantially modify the dynamic response of the structure and, therefore, should be incorporated into the mathematical model.

In the proposed formulation, the beam is described by a system of nonlinear differential equations that combines the shear deformation effects characteristic of the Timoshenko theory with the axial deformation mechanisms of the Gao beam model [26]. The static version of this combined formulation has been discussed in [27,28]. The interaction between shear deformation, axial forces, and inertial moving loads leads to qualitative and quantitative modifications of the system response.

The remainder of this paper is organised as follows. Section 2 presents the dynamic formulation of the problem. The resulting model consists of two strongly nonlinear hyperbolic partial differential equations with appropriate initial and boundary conditions. The numerical scheme is described in Sections 3 and 4. Implementation details and simulation results are discussed in Section 5. Finally, Section 6 summarises the main findings and presents the conclusions of the study.

2. Mathematical model

In this section, a dynamic extended Gao beam model with a moderately thick cross-section, subjected to a moving inertial point load, is formulated. The physical scheme of the analysed system is presented in Fig. 1.

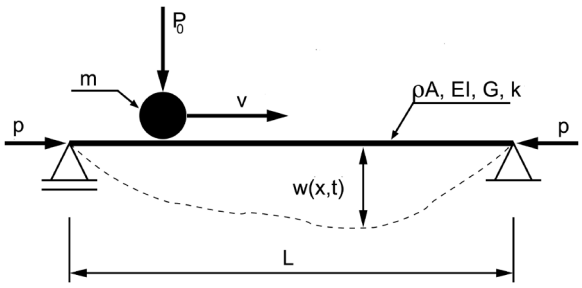

Fig. 1. Geometric scheme of the beam and the assumed load configuration.

The mathematical model is based on the assumption of nonlinear, relatively large displacements combined with small strains (within the framework of small plane strain theory). The reference configuration of the beam with length L, thickness $2h$, and width d_e, corresponding to the undeformed state, is defined in a rectangular Cartesian coordinate system (x, y, z) as the domain D

$$\mathsf{D} = \{(x, y, z) : 0 \le x \le L, -h \le y \le h, 0 \le z \le d_e\}\,.$$

The origin of the coordinate system ($x = 0$) is located at the geometric centre of the left end of the beam. The beam is subjected to a constant axial compressive force p. This force constitutes a key control parameter, the critical value of which may lead to the loss of stability of the system (buckling). Furthermore, a transverse concentrated force P_0 acts on the structure, associated with a mass m moving along the beam with a constant velocity v.

The following material and geometric parameters are adopted (cf. Fig. 1): E denotes Young's modulus, ν is Poisson's ratio, G represents the shear modulus (Kirchhoff's modulus), $A = 2hd_e$ is the cross-sectional area, $I = \frac{2}{3}h^3 d_e$ denotes the moment of inertia of the cross-section, ρ is the material density, and k constitutes the shear correction factor.

The applied thick Gao beam model is a development of the concept presented in paper [27], originally developed for static problems. This model allows for the description of the behaviour of moderately thick beams, taking into account shear effects and geometric nonlinearity.

The primary difference between a thin and a thick beam lies in how shear deformations influence their behaviour under a load. In thin beams (Bernoulli-Euler model), it is assumed that cross-sections remain perpendicular to the bending axis, effectively ignoring the effects of shear. Conversely, thick beams (Timoshenko model) account for additional deformations caused by transverse shear forces, resulting in greater calculated deflections. In engineering, the thin beam model is used for slender elements (length-to-depth ratio $>$ 20:1), while the thick beam model is necessary when the beam's height is significant relative to its span (length-to-depth ratio $<$ 10:1, or the so-called "medium" model for ratios between 10 and 20).

Using simplified notation, where partial derivatives with respect to the coordinate x or time t are denoted by a subscript (e.g., $f_{,x} \equiv \partial f/\partial x$), the system of equations of motion for the Gao beam subjected to a moving inertial load takes the form

$$\rho A w_{,tt} - \frac{GA}{k}(w_{,xx} - \theta_{,x}) + p\, w_{,xx} = \delta(x - vt)P_0 - \delta(x - vt)m\frac{\mathrm{d}^2 w(vt, t)}{\mathrm{d}t^2}\,, \tag{1}$$

$$\rho I \theta_{,tt} - EI\,\theta_{,xx} - \frac{GA}{k}(1 - \nu^2)(w_{,x} - \theta) + \frac{1}{2}EA(1 - \nu^2)\,\theta^3 - \nu(1 - \nu^2)\,p\,\theta = 0\,. \tag{2}$$

In the system described by (1)-(2), the kinematic state is defined by the vertical displacement (deflection) of the neutral axis $w(x, t)$ and the rotation angle of the cross-section $\theta(x, t)$, which accounts for the combined effects of pure bending and shear deformation. The physical and geometric characteristics of the beam are represented by the Young's modulus E, shear modulus G, Poisson's ratio ν, and density ρ, along with the cross-sectional area A, the area moment of inertia I, and the shear correction factor k. Furthermore, the model incorporates a compressive axial force p and a moving load assembly. This assembly consists of a concentrated mass m and a force P_0 acting at the tracking point $(x - vt)$, both of which are applied as point loads through the use of the Dirac delta function δ. This approach represents concentrated loads as distributions, enabling their inclusion in the continuous equations of motion. Specifically, the sifting property defines the load's space-time variation, integrating the excitation directly into the governing differential operator. Eqs. (1)-(2) in the above form, though without the term describing the influence of the moving load, were derived in the paper [28]. A more detailed analysis of the stages of their derivation can be found in the work [27]. The mathematical formulation of the system's dynamics is established through two coupled differential equations that provide a complementary description of the mechanical processes within the structure. Eq. (1) characterises the temporal evolution of transverse vibrations, accounting for translational inertia, coupling effects with shear deformation, and the influence of the external axial load. The right-hand side of this expression defines the external excitation vector arising directly from the interaction of the moving load components. In parallel, Eq. (2) governs the rotational dynamics of the cross-section by integrating fundamental inertial and stiffness parameters. This formulation incorporates rotational inertia, bending stiffness, and shear coupling, supplemented by the contribution of the axial force. A distinctive feature of the thick Gao beam model is the inclusion of a nonlinear cubic term θ^3 in Eq. (2), which facilitates a precise representation of geometrically nonlinear effects in the strain state analysis.

The system of Eqs. (1)-(2) can be transformed into a normalized form by introducing key physical quantities of the Timoshenko beam theory, namely the characteristic wave propagation velocities. The fundamental wave velocities known from Timoshenko beam

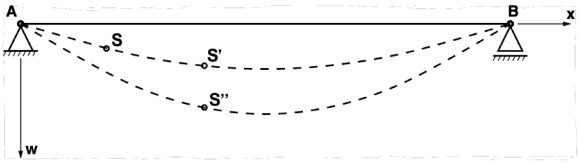

Fig. 2. Geometric interpretation of the Renaudot formula for determining the acceleration of the moving mass.

theory have been introduced

$$c_G^2 = \frac{G}{\rho k}, \quad c_E^2 = \frac{E}{\rho},$$

where c_G is the shear wave propagation velocity, and c_E is the longitudinal (tensile/compressive) wave velocity. For clarity and universality of the analysis, the following reduced (with respect to density and cross-sectional area) load-related quantities are defined:

$$\widetilde{p} = \frac{p}{\rho A}, \quad \widetilde{P}_0 = \frac{P_0}{\rho A}, \quad \widetilde{m} = \frac{m}{\rho A}.$$

Finally, we obtain a clear system of equations in the following normalised form

$$w_{,tt} - c_G^2 (w_{,xx} - \theta_{,x}) + \widetilde{p}\, w_{,xx} = \delta(x - vt)\widetilde{P}_0 - \delta(x - vt)\widetilde{m}\frac{\mathrm{d}^2 w(vt,t)}{\mathrm{d}t^2}, \tag{3}$$

$$\theta_{,tt} - c_E^2\, \theta_{,xx} - \frac{3}{h^2} c_G^2 (1-\nu^2)(w_{,x} - \theta) + \frac{3}{2h^2} c_E^2 (1-\nu^2)\theta^3 - \frac{3}{h^2}\widetilde{p}\,\nu(1-\nu^2)\,\theta = 0. \tag{4}$$

This normalisation allows for direct comparison of dynamic and static effects and provides a clearer identification of control parameters in the study of the beam's response under a moving load, particularly in the context of resonance phenomena and wave propagation.

The system of equations is supplemented by boundary conditions. For a beam simply supported at both ends, they take the form

$$w(0) = 0\,, \quad w(L) = 0\,, \quad \theta_{,x}(0) = 0\,, \quad \theta_{,x}(L) = 0\,, \tag{5}$$

and homogeneous initial conditions

$$w(x,0) = 0\,, \quad w_{,t}(x,0) = 0\,, \quad \theta(x,0) = 0\,, \quad \theta_{,t}(x,0) = 0\,. \tag{6}$$

A significant aspect of the presented problem is the modelling method of the moving load. Treating it solely as a constant gravitational force is admissible only for low velocities. The literature indicates that as the velocity v increases, inertial effects associated with the trajectory of the mass m begin to play a dominant role, which alters the dynamic response of the entire system. Neglecting these effects leads to significant qualitative and quantitative errors.

To correctly account for the load dynamics, the second derivative of the vertical displacement of the contact point $w(vt,t)$ is written using the material (total) derivative. Assuming a constant velocity v, the so-called Renaudot formula is obtained [29]

$$\frac{\mathrm{d}^2 w(vt,t)}{\mathrm{d}t^2} = w_{,tt}\big|_{x=vt} + 2v\, w_{,xt}\big|_{x=vt} + v^2\, w_{,xx}\big|_{x=vt}\,. \tag{7}$$

A geometric interpretation of the components of the above formula is presented in Fig. 2.

Consider the load located at point S at time t. During an infinitesimal time increment $\mathrm{d}t$, assuming a hypothetical, "frozen" deflection profile of the beam (line AB), the mass would displace to point S'. However, due to the system dynamics, the beam profile evolves simultaneously, resulting in the final load position at S". This implies that the total displacement is a superposition of changes resulting from both motion along the x-coordinate and time evolution t. Consequently, determining the actual vertical acceleration of the moving mass requires the application of the total (material) derivative of the composite function w.

The term $w_{,tt}$ represents the vertical acceleration of the beam itself at the contact point, $2v\, w_{,xt}$ corresponds to the Coriolis acceleration, and $v^2\, w_{,xx}$ constitutes the centrifugal force component resulting from the curvature of the trajectory along which the mass moves. The necessity of applying the total derivative stems from the fact that during time $\mathrm{d}t$, both the time and the position of the load on the deformed beam change (transition from point S to S").

In summary, the presented model consists of a system of two coupled, nonlinear partial differential equations. It constitutes a generalisation of the classical Timoshenko beam theory, extending it with nonlinear effects and full consideration of the moving load inertia. The linear part of the model aligns with Timoshenko theory, ensuring consistency with classical solutions for small displacements. If shear is neglected, the model reduces to the canonical Gao beam form [26].

3. Numerical model of a thick Gao beam

Analytical or closed solutions in the case of this nonlinear problem are generally unavailable. Numerical approximations of the two coupled equations are obtained through the implementation of the finite element method. The beam is divided into n equal finite elements of length b. The interval of a finite element is represented by $\Omega = \{x : 0 \le x \le b\}$. In the subsequent steps and the derivation

of the finite element matrix, we proceed classically, applying the weak variational formulation. A linear interpolation $\mathbf{N}$ of the nodal values $\mathbf{w}$ and $\boldsymbol{\theta}$ of the finite element, containing generalised displacements, i.e., lateral displacements and rotations at both element ends, is applied independently for lateral displacements w and rotations θ

$$w(x) = \mathbf{N}\mathbf{w}, \qquad \theta(x) = \mathbf{N}\boldsymbol{\theta}, \tag{8}$$

where

$$\mathbf{N} = \begin{bmatrix} 1 - \dfrac{x}{b} & \dfrac{x}{b} \end{bmatrix}, \tag{9}$$

together with

$$\mathbf{w} = \begin{bmatrix} w_L & w_R \end{bmatrix}^{\mathsf{T}}, \qquad \boldsymbol{\theta} = \begin{bmatrix} \theta_L & \theta_R \end{bmatrix}^{\mathsf{T}}.$$

These functions have a fundamental property: for $x = 0$ the first term equals 1 and the second 0, which corresponds to the value at the left node of the element, while for $x = b$ the situation is reversed - the first term equals 0 and the second 1, representing the value at the right node. Between the nodes, the variation is strictly linear along the element. A key aspect is the independent interpolation of deflection w and rotation angle θ, which is characteristic of Timoshenko beam theory that accounts for shear deformations. This constitutes an essential difference compared to Bernoulli-Euler theory, where it is assumed that $\theta = dw/dx$, i.e., the rotation angle of the cross-section is directly related to the derivative of deflection.

Virtual functions, specifically the virtual displacement $w^*(x)$ and virtual rotation angle $\theta^*(x)$ used in the weak formulation, are denoted by an asterisk. These differ from the actual functions in that they must vanish at the boundaries where essential (Dirichlet) conditions are prescribed. Consequently, the physical boundary conditions are sufficient to perform integration by parts. Let $\mathbf{N}^*$ represent the virtual interpolation functions, while $\mathbf{w}^*$ and $\boldsymbol{\theta}^*$ denote the virtual nodal parameters. The final interpolation is then expressed as

$$w^*(x) = \mathbf{N}^*\,\mathbf{w}^*, \qquad \theta^*(x) = \mathbf{N}^*\,\boldsymbol{\theta}^*, \tag{10}$$

and

$$w^* = 0 \;\text{ and }\; \theta^* = 0, \quad \text{for } x = 0 \text{ and } b. \tag{11}$$

The virtual functions $\mathbf{N}^*$ were taken to be identical to $\mathbf{N}$, vanishing at the boundaries of the interval $[0, b]$. Functions (10) do not necessarily have to vanish where natural (Neumann) conditions are set; in fact, their presence there is what allows us to incorporate “forces” or “fluxes” into the equation.

The assumption that the virtual displacements w^* and θ^* vanish on the element boundaries (for $x = 0$ and b) follows directly from the principle of virtual work applied in the finite element method. This crucial assumption serves several important roles in the problem formulation. First, it guarantees the continuity of the solution between adjacent elements in the discretisation, which is a fundamental requirement of the method. Second, it allows for the elimination of boundary terms that appear in the integration by parts process during the derivation of the weak form of the equations. Third, it ensures that the internal forces on the boundaries of individual elements are properly transferred through the nodes to adjacent elements, which enables proper assembly of the global system matrix.

In order to derive the characteristic matrices describing the discretised system, the weak form of the equations, also called the variational formulation, is used. The equations are multiplied by virtual displacements and virtual angles, respectively, and both equations are integrated over the area of the element domain Ω. In this part, we deal with the components of equations related to the beam. The numerical description of the moving point mass will be presented in a separate section of the manuscript.

Finally, the virtual work equations can be written in the following form

$$\Pi_w^* = \int_\Omega w^* \left\{ \rho A w_{,tt} - \frac{GA}{k}(w_{,xx} - \theta_{,x}) + p w_{,xx} \right\} \mathrm{d}\Omega, \tag{12}$$

$$\Pi_\theta^* = \int_\Omega \theta^* \left\{ \rho I\, \theta_{,tt} - E I\, \theta_{,xx} - \frac{GA}{k}(1-\nu^2)(w_{,x} - \theta) + \frac{1}{2} E A (1-\nu^2)\, \theta^3 - \nu(1-\nu^2) p\, \theta \right\} \mathrm{d}\Omega. \tag{13}$$

For the deflection w, the virtual work equation contains three main components with clear physical interpretation. The first term, $\rho A\, w_{,tt}$, represents the inertia forces acting on the element, being the product of mass per unit length and transverse acceleration. The second term, $(GA/k)(w_{,xx} - \theta_{,x})$, describes the shear force according to Timoshenko theory, where GA denotes the shear stiffness of the cross-section, k is the shear correction coefficient (typically taken as 5/6 for rectangular cross-section), and the expression $w_{,xx} - \theta_{,x}$ represents the difference between the curvature of deflection and the slope of the cross-section, constituting a direct measure of shear deformation. The third term, $p\, w_{,xx}$, describes the influence of axial force p on the element stiffness, representing an essential geometric effect that can lead to the phenomenon of buckling under compressive force.

The equation for rotation θ is more complex and contains a larger number of components. The term $\rho I\, \theta_{,tt}$ represents the rotational inertia moment, where I is the moment of inertia of the cross-section. The term $E I\, \theta_{,xx}$ describes the bending moment. As the product of Young’s modulus and the moment of inertia, it represents the classical bending stiffness. The next component, $(GA/k)(1-\nu^2)(w_{,x} - \theta)$, describes the coupling with shear deformation, where the factor $(1-\nu^2)$ accounts for the Poisson effect in a plane stress state. Particularly interesting is the nonlinear term $Eh(1-\nu^2)\,\theta^3$, which introduces cubic nonlinearity with respect to the rotation angle and is related to large rotation effects. The last term, $\nu(1-\nu^2)p\,\theta$, represents the coupling between the acting axial force and the rotation of the cross-section, which is essential in structural stability analysis.

Substituting the interpolation expressions into the virtual work equations and integrating by parts, we obtain the following form of virtual work equations, taking into account shape functions

$$\Pi_w^* = (\mathbf{w}^*)^{\mathsf{T}} \int_\Omega \left\{ \rho A\, (\mathbf{N}^*)^{\mathsf{T}} \mathbf{N} \mathbf{w}_{,tt} + \frac{GA}{k} \left[(\mathbf{N}_{,x}^*)^{\mathsf{T}} \mathbf{N}_{,x} \mathbf{w} + (\mathbf{N}^*)^{\mathsf{T}} \mathbf{N}_{,x} \boldsymbol{\theta} \right] - p\, (\mathbf{N}_{,x}^*)^{\mathsf{T}} \mathbf{N}_{,x} \mathbf{w} \right\} \mathrm{d}\Omega\,, \tag{14}$$

$$\begin{aligned} \Pi_\theta^* = (\boldsymbol{\theta}^*)^{\mathsf{T}} \int_\Omega \Big\{ & \rho I\, (\mathbf{N}^*)^{\mathsf{T}} \mathbf{N} \boldsymbol{\theta}_{,tt} + EI\, (\mathbf{N}_{,x}^*)^{\mathsf{T}} \mathbf{N}_{,x} \boldsymbol{\theta} - \frac{GA}{k}(1-\nu^2) \left[(\mathbf{N}^*)^{\mathsf{T}} \mathbf{N}_{,x} \mathbf{w} - (\mathbf{N}^*)^{\mathsf{T}} \mathbf{N} \boldsymbol{\theta} \right] \\ & + \frac{1}{2} EA(1-\nu^2)\, (\mathbf{N}^*)^{\mathsf{T}} (\mathbf{N}\boldsymbol{\theta})^2 \mathbf{N} \boldsymbol{\theta} - \nu(1-\nu^2) p\, (\mathbf{N}^*)^{\mathsf{T}} \mathbf{N} \boldsymbol{\theta} \Big\} \mathrm{d}\Omega\,. \end{aligned} \tag{15}$$

The matrices $\mathbf{N}$ and $\mathbf{N}^*$ represent the shape functions and their virtual counterparts. In the present formulation, linear interpolation polynomials are used to approximate the transverse displacement $\mathbf{w}$ and the rotation $\boldsymbol{\theta}$ within the element in terms of the nodal degrees of freedom (9).

In order to derive the characteristic matrices, the energy is minimised with respect to the virtual variables, which reduces to equating the partial derivatives of the functionals with respect to the virtual increments of deflections and rotation angles to zero, in accordance with the following relation

$$\frac{\partial \Pi_w^*}{\partial (\mathbf{w}^*)^{\mathsf{T}}} = \mathbf{0}\,, \qquad \frac{\partial \Pi_\theta^*}{\partial (\boldsymbol{\theta}^*)^{\mathsf{T}}} = \mathbf{0}\,.$$

This condition ensures that the sought solution corresponds to the equilibrium state of the system. As a result of integrating simple polynomials serving as shape functions, the equation describing the transverse displacement field (14) takes the following matrix form

$$\rho Ab \begin{bmatrix} 1/3 & 1/6 \\ 1/6 & 1/3 \end{bmatrix} \mathbf{w}_{,tt} + \frac{GA}{kb} \begin{bmatrix} 1 & -1 \\ -1 & 1 \end{bmatrix} \mathbf{w} + \frac{GA}{k} \begin{bmatrix} -1/2 & 1/2 \\ -1/2 & 1/2 \end{bmatrix} \boldsymbol{\theta} - \frac{p}{b} \begin{bmatrix} 1 & -1 \\ -1 & 1 \end{bmatrix} \mathbf{w} = \mathbf{0}\,, \tag{16}$$

Proceeding to the analysis of rotations, it is necessary to account for geometric nonlinearities. Denoting the rotation angle at the left and right nodes of the finite element by θ_L and θ_R, respectively, the nonlinear relation $(\mathbf{N}\boldsymbol{\theta})^2$ can be written in the following explicit form, resulting from the quadratic combination of shape functions

$$(\mathbf{N}\boldsymbol{\theta})^2 = \left(1 - \frac{x}{b}\right)^2 \theta_L^2 + 2\frac{x}{b}\left(1 - \frac{x}{b}\right)\theta_L \theta_R + \frac{x^2}{b^2}\theta_R^2\,. \tag{17}$$

This relation is essential for the correct formulation of the strain energy in the presence of large rotations. After performing the necessary variational transformations and incorporating the expansion (17), the moment equilibrium Eq. (15) takes the following form

$$\begin{aligned} & \rho Ib \begin{bmatrix} 1/3 & 1/6 \\ 1/6 & 1/3 \end{bmatrix} \boldsymbol{\theta}_{,tt} + \frac{EI}{b} \begin{bmatrix} 1 & -1 \\ -1 & 1 \end{bmatrix} \boldsymbol{\theta} - \frac{GA}{k}(1-\nu^2) \begin{bmatrix} -1/2 & 1/2 \\ -1/2 & 1/2 \end{bmatrix} \mathbf{w} + \frac{GA}{k}(1-\nu^2) \begin{bmatrix} 1/3 & 1/6 \\ 1/6 & 1/3 \end{bmatrix} \boldsymbol{\theta} \\ & + \frac{EA(1-\nu^2)b}{120} \begin{bmatrix} 12\theta_L^2 + 6\theta_L\theta_R + 2\theta_R^2 & 3\theta_L^2 + 4\theta_L\theta_R + 3\theta_R^2 \\ 3\theta_L^2 + 4\theta_L\theta_R + 3\theta_R^2 & 2\theta_L^2 + 6\theta_L\theta_R + 12\theta_R^2 \end{bmatrix} \boldsymbol{\theta} - \nu(1-\nu^2) pb \begin{bmatrix} 1/3 & 1/6 \\ 1/6 & 1/3 \end{bmatrix} \boldsymbol{\theta} = \mathbf{0}\,. \end{aligned} \tag{18}$$

Based on the previously derived components, the entire problem under consideration can be expressed using the following matrix formulation, which constitutes the foundation of the dynamic analysis

$$\mathbf{M}\mathbf{Q}_{,tt} + \mathbf{K}\mathbf{Q} = \mathbf{0}\,, \tag{19}$$

where the vector of nodal values, grouping all degrees of freedom of the element, is defined as

$$\mathbf{Q} = \begin{bmatrix} w_L & \theta_L & w_R & \theta_R \end{bmatrix}^{\mathsf{T}}. \tag{20}$$

The integrals obtained in this way and the resulting matrices contain a complete physical description of the phenomenon, integrating contributions from inertia (both translational and rotational), bending and shear stiffness, as well as significant geometric effects induced by the axial load p and nonlinear effects associated with large rotations.

The inertia matrix $\mathbf{M}$ takes the form of a so-called consistent mass matrix, as opposed to simpler lumped mass matrices. The matrix can be given in the following form

$$\mathbf{M} = \rho \frac{b}{6} \begin{bmatrix} 2A & 0 & A & 0 \\ 0 & 2I & 0 & I \\ A & 0 & 2A & 0 \\ 0 & I & 0 & 2I \end{bmatrix}, \qquad I = \iint_A y^2\, dA\,. \tag{21}$$

It is multiplied by the coefficient $\rho b/6$, where ρ is the material density, b is the element length, and 6 appears as a result of integrating the products of linear shape functions. The matrix structure exhibits a clear 2×2 block form. In each block, the first diagonal element

corresponds to the translational mass associated with the cross-sectional area A, while the second represents the rotational inertia related to the second moment of area I, which is defined as the double integral over the cross-section. A characteristic feature of this matrix is the ratio between diagonal and off-diagonal elements - the diagonal elements equal $2A$ and $2I$, while the corresponding off-diagonal elements are A and I, giving a 2:1 ratio. These proportions result directly from integrating the products of linear shape functions over the element domain. A very important aspect of the structure of matrix $\mathbf{M}$ is the lack of coupling between deflection w and rotation θ, which manifests through zeros in the off-diagonal positions between blocks. This means that the translational mass and rotational inertia are treated as independent.

The stiffness matrix $\mathbf{K}$ of the finite beam element is a sum of four components

$$\mathbf{K} = \mathbf{K}_s + \mathbf{K}_b + \mathbf{K}_p + \mathbf{K}_n \,. \tag{22}$$

Each of these matrices represents a different physical aspect of beam behaviour. Such decomposition facilitates both the understanding of physical phenomena and numerical implementation, since individual matrices can be computed and assembled independently.

The first matrix is the shear stiffness matrix $\mathbf{K}_s$ with the following form

$$\mathbf{K}_s = \frac{GA}{k}\begin{bmatrix} 1/b & -1/2 & -1/b & 1/2 \\ (1-\nu^2)/2 & (1-\nu^2)b/3 & -(1-\nu^2)/2 & (1-\nu^2)b/6 \\ -1/b & -1/2 & 1/b & 1/2 \\ (1-\nu^2)/2 & (1-\nu^2)b/6 & -(1-\nu^2)/2 & (1-\nu^2)b/3 \end{bmatrix}. \tag{23}$$

The matrix $\mathbf{K}_s$, with the multiplier GA/k, represents the shear stiffness of the cross-section, a key element of the Timoshenko theory. Particularly interesting is the appearance of the coefficient $1-\nu^2$ in the rows and columns associated with the rotation angle θ, which accounts for the Poisson effect in a plane stress state. Terms of the type $1/b$ in the matrix indicate an important property that the shear stiffness increases as the element becomes shorter, which has an intuitive physical justification.

The second matrix is the bending stiffness matrix $\mathbf{K}_b$ with the following form

$$\mathbf{K}_b = \frac{EI}{b}\begin{bmatrix} 0 & 0 & 0 & 0 \\ 0 & 1 & 0 & -1 \\ 0 & 0 & 0 & 0 \\ 0 & -1 & 0 & 1 \end{bmatrix}. \tag{24}$$

The matrix $\mathbf{K}_b$, multiplied by the ratio EI/b, represents the classical bending stiffness of the beam. Its structure is particularly simple - nonzero elements appear in the rows and columns associated with displacement w (the first and third degrees of freedom). The structure of the 2×2 block associated with rotations has the typical form of a difference matrix $[1, -1; -1, 1]$, which is characteristic of the second-order differential operator. The coefficient EI/b shows that the longer the element, the smaller its bending stiffness, which again has a clear mechanical justification.

The third matrix is the geometric stiffness matrix $\mathbf{K}_p$ with the following form

$$\mathbf{K}_p = p\begin{bmatrix} -1/b & 0 & 1/b & 0 \\ 0 & -\nu(1-\nu^2)b/3 & 0 & -\nu(1-\nu^2)b/6 \\ 1/b & 0 & -1/b & 0 \\ 0 & -\nu(1-\nu^2)b/6 & 0 & -\nu(1-\nu^2)b/3 \end{bmatrix}. \tag{25}$$

The matrix $\mathbf{K}_p$, directly multiplied by the value of axial force p, represents the so-called geometric effect, also known as the geometric matrix. This matrix has fundamental significance in structural stability analysis. When the force p is positive, which corresponds to tension, this matrix increases the total stiffness of the system, whereas for a negative force, representing compression, it decreases the stiffness, which can lead to loss of stability in the form of buckling. Terms containing $-\nu(1-\nu^2)b/3$ and $-\nu(1-\nu^2)b/6$ in the rows associated with rotations θ describe the influence of axial force on rotational components, which is particularly important in flexural-torsional buckling analysis.

The fourth and final component matrix is the nonlinear stiffness matrix $\mathbf{K}_n$ with the following form

$$\mathbf{K}_n = \frac{EA(1-\nu^2)b}{120}\begin{bmatrix} 0 & 0 & 0 & 0 \\ 0 & 12\theta_L^2 + 6\theta_L\theta_R + 2\theta_R^2 & 0 & 3\theta_L^2 + 4\theta_L\theta_R + 3\theta_R^2 \\ 0 & 0 & 0 & 0 \\ 0 & 3\theta_L^2 + 4\theta_L\theta_R + 3\theta_R^2 & 0 & 2\theta_L^2 + 6\theta_L\theta_R + 12\theta_R^2 \end{bmatrix}. \tag{26}$$

The matrix $\mathbf{K}_n$ is the most complex component because it introduces nonlinearity to the problem. It is multiplied by the coefficient $EA(1-\nu^2)b/120$ and contains terms dependent on the current values of rotation angles at the nodes - θ_L for the left node and θ_R for the right node. The matrix elements contain combinations of squares and products of these angles, such as $12\theta_L^2$, $6\theta_L\,\theta_R$, or $2\theta_R^2$, which originate from the integration of the cubic term θ^3 appearing in the variational equation. This matrix has nonzero elements

for the degrees of freedom associated with the rotation angle θ. The presence of matrix $\mathbf{K}_n$ requires the use of iterative methods in the solution process, since the stiffness matrix depends on the solution itself.

The final equation of motion (19) represents a nonlinear system of second-order ordinary differential equations describing the dynamics of the discretised system. The vector $\mathbf{Q}$ contains all nodal degrees of freedom - deflections and rotations - and is a function of time. The first term of the equation, $\mathbf{MQ}_{,tt}$, represents the inertia forces present in the system, being the product of the mass matrix and the acceleration vector. The second term, $\mathbf{KQ}$, represents the elastic and nonlinear forces acting in the structure.

A fundamental feature of this equation is its nonlinearity, resulting from the fact that the stiffness matrix $\mathbf{K}$ contains the component $\mathbf{K}_n$, which depends on the current values of the solution $\mathbf{Q}$. This nonlinearity has far-reaching consequences for the solution properties and methods of determination. First, the principle of superposition does not apply, which means that the sum of two solutions is not a solution of the system. Second, the vibration amplitude directly affects the natural frequencies of the system - in contrast to linear systems, where frequencies are constant and independent of amplitude. Third, complex nonlinear phenomena may occur in the system, such as bifurcations, subharmonic and superharmonic resonances, and even chaotic behaviour for certain parameter ranges. Fourth, the solution process requires the use of iterative methods at each time step, since the stiffness matrix must be updated based on the current approximation of the solution.

4. Numerical model of a moving mass

To derive the characteristic matrices describing the moving load, the weak form of the equations was employed. According to Renaudot's formula (7), the part of Eq. (1) concerning the moving point mass m and the moving point force P_0 was used.

Ultimately, the virtual work equation for a moving point load can be written in the following form

$$\Pi_w^* = \int_\Omega w^* \left\{ \delta(x - vt)\left(P_0 - m w_{,tt} - 2mv w_{,xt} - mv^2 w_{,xx} \right) \right\} \mathrm{d}\Omega \,. \tag{27}$$

The integral extends over the element domain Ω, which enables application of the finite element method to the moving load problem. The symbol w^* denotes the virtual displacement, i.e., a test function consistent with the principle of virtual work. The Dirac delta $\delta(x - vt)$ localises the load at a point moving with velocity v according to the relation $x = vt$. The expression in curly brackets defines the complete set of forces acting at the contact point between the load and the beam: the external force P_0, the inertia force $mw_{,tt}$ (resulting from mass acceleration), the Coriolis force $2mvw_{,xt}$ (associated with the motion of mass on a deforming structure), and the centrifugal force $mv^2 w_{,xx}$ (arising from motion along the curved trajectory of the deflected beam).

Renaudot's formula presented in Section 2 provides a complete mathematical description of a point mass moving with constant velocity v. However, the application of linear shape functions encounters significant difficulties. These arise from the fact that these functions enable accurate representation of only the first derivative of displacement, whereas the equation contains second derivatives, and the Dirac delta localises the load. The standard integration by parts procedure, employed to reduce the order of derivatives in the weak formulation, encounters serious mathematical problems in this case due to the presence of the Dirac delta.

A solution to this problem is offered by the modified Renaudot's formula, given in Eq. (28), which decomposes the total time derivative of acceleration for a point moving with velocity v along the beam in the following form

$$\frac{\mathrm{d}^2 w(vt,t)}{\mathrm{d}t^2} = w_{,tt}\big|_{x=vt} + v\, w_{,xt}\big|_{x=vt} + v \frac{\mathrm{d}}{\mathrm{d}t}\left[w_{,x}\big|_{x=vt} \right] . \tag{28}$$

The left side of the equation describes the actual vertical acceleration experienced by a particle moving at a constant velocity v along the structure. The right side contains three terms: local vertical acceleration associated with the beam's vibration at a fixed point, the convective term resulting from the mass moving through a field of changing vibration velocity, and the rate of slope change. The second term, together with the first part of the expanded third term, contributes to the Coriolis component ($2vw_{,xt}$). The remaining part of the expanded third term corresponds to the centrifugal acceleration ($v^2 w_{,xx}$), which arises from the particle moving along the curvature of the beam.

The key advantage of formula (28) is that all three components on the right side can be treated as independent quantities in the finite element method. This allows avoiding direct differentiation of the Dirac delta and enables the use of linear shape functions. This approach, originally presented in work [30], constitutes a significant contribution to the numerical analysis of dynamics problems with moving loads. Application of formula (28) in the energy minimisation process, described by the virtual work Eq. (27), leads to obtaining characteristic matrices representing the moving mass.

We introduce a local dimensionless parameter κ ($0 \le \kappa \le 1$), which specifies the spatial location of the concentrated mass m along the span of a finite element of length b defined over the interval $[x_L, x_R]$. $\kappa = (x - x_L)/b$ and varies from 0 to 1. The mass matrix $\mathbf{M}_m$ of a single finite element representing the influence of a point mass m has the following form:

$$\mathbf{M}_m = m \begin{bmatrix} (1-\kappa)^2 & 0 & \kappa(1-\kappa) & 0 \\ 0 & 0 & 0 & 0 \\ \kappa(1-\kappa) & 0 & \kappa^2 & 0 \\ 0 & 0 & 0 & 0 \end{bmatrix} . \tag{29}$$

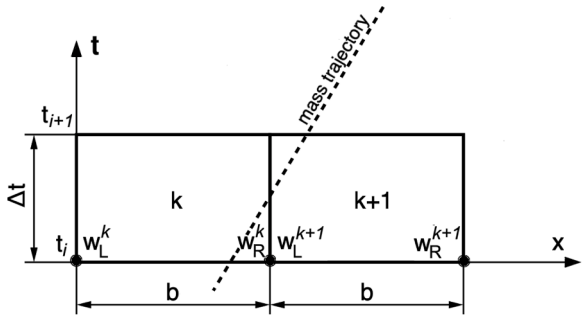

Fig. 3. The moving mass transition between finite element k and $k+1$.

This matrix, of dimensions 4x4, corresponds to a beam element with two nodes and two degrees of freedom per node (deflection, rotation). It acts only on degrees of freedom corresponding to deflections (first and third). The parameter $\kappa \in [0,1]$ determines the position of the mass within the element. The matrix $\mathbf{M}_m$ is symmetric, and the sum of elements in columns corresponding to deflections equals m, which ensures conservation of total mass.

The damping matrix $\mathbf{C}_m$ representing the Coriolis effect has the following form

$$\mathbf{C}_m = \frac{2mv}{b}\begin{bmatrix} \kappa-1 & 0 & 1-\kappa & 0 \\ 0 & 0 & 0 & 0 \\ -\kappa & 0 & \kappa & 0 \\ 0 & 0 & 0 & 0 \end{bmatrix}. \tag{30}$$

The structure of this matrix is antisymmetric, which is characteristic of gyroscopic forces. The multiplier $2mv/b$ directly results from Coriolis acceleration. The sum of elements in each row equals zero, which reflects the fact that Coriolis forces do no work.

The vector $\mathbf{e}_m^t$ representing the centrifugal effect has the form

$$\mathbf{e}_m^t = \frac{mv}{b\,\Delta t}\begin{bmatrix} (1-\kappa)\left(w_R^{k+1} - w_R^k - w_L^{k+1} + w_L^k\right) \\ 0 \\ \kappa\left(w_R^{k+1} - w_R^k - w_L^{k+1} + w_L^k\right) \\ 0 \end{bmatrix}. \tag{31}$$

This vector models the centrifugal force dependent on beam curvature.

As long as the mass transit within the time step Δt begins and ends within the same spatial element, the nodal forces described by Eq. (31) are easy to define. In the case shown in Fig. 3, where the mass transit begins in element 'k' and ends in the subsequent element '$k+1$' after time Δt, the nodal forces $\mathbf{e}_m^t$ must be calculated according to the previous formulation. The difference lies in the fact that the nodal forces are determined based on the nodal displacements of both elements. w_L^k and w_R^k are the displacements of both nodes of the preceding element 'k', while w_L^{k+1} and w_R^{k+1} are the displacements of element '$k+1$'. The displacements w_R^k and w_L^{k+1} are the same displacements. They have been denoted separately because it allows for a simpler formulation of Eq. (31) for the purpose of computational implementation. A single formula then covers both the case of mass transit within a single element and the transit from one element to another.

The expression $\left(w_R^{k+1} - w_R^k - w_L^{k+1} + w_L^k\right)$ constitutes a discrete approximation of the second spatial derivative $w_{,xx}$, calculated based on deflection values at nodes of adjacent elements (k and $k+1$). The graphical interpretation of the mass transition between finite element k and $k+1$ is presented in Fig. 3.

The coefficients $1-\kappa$ and κ distribute the force to the nodes. This vector must be updated at each time step.

The moving force vector $\mathbf{F}^t$ has the form

$$\mathbf{F}^t = P_0\begin{bmatrix} 1-\kappa \\ 0 \\ \kappa \\ 0 \end{bmatrix}. \tag{32}$$

It represents the distribution of the constant concentrated force P_0 to the element nodes according to linear shape functions. The sum of vector components equals P_0, which ensures conservation of total force.

In all the above matrices, a key role is played by the parameter κ, which changes continuously in time $\kappa = (vt - x_L)/b$, where x_L is the coordinate of the first node of the element. When the load moves through successive mesh elements, the value of κ resets to

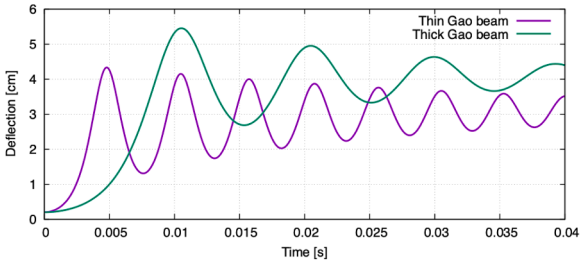

Fig. 4. Comparison of a thin (Bernoulli-Euler-like) and a thick (Timoshenko-like) models of Gao beam compressed with a force $p = 575$ kN, small damping $c = 50$ Ns/m.

zero for each new element. At any given instant, only one element has a nonzero matrix associated with the moving load. The value of κ influences the distribution of loads and the intensity of dynamic effects; for example, the influence of mass on a node is maximal when the mass is located at the node ($\kappa = 0$ or 1), while inter-nodal coupling reaches its maximum for $\kappa = 0.5$.

The modelling of the system's dynamics begins with the aggregation of the beam's elemental matrices, defined in (21), (23)–(26), into global inertia and stiffness matrices. These establish the fundamental structural characteristics, which are then supplemented by the effects of a moving point mass. Due to the time-varying position of the load, the resulting system of differential equations has non-constant coefficients and must be updated iteratively at each discrete time step. The interaction of the moving mass is introduced via the matrix contributions (29) and (30), and the vector (31), projected onto the global degrees of freedom according to the current position along the beam. This yields a time-dependent system in which the inertia and damping matrices evolve with the mass motion. Simultaneously, the global force vector is updated by relocating the components of (31) in line with the kinematics of the excitation. The structural damping matrix is assumed to be zero and Coriolis-like effects are introduced locally through successive contributions from the moving load, represented by (30). This procedure defines a complete algorithm for assembling the matrix equations, enabling numerical integration of the system's dynamic response in the time domain.

5. Results

This section presents the key results obtained from numerical simulations, aimed at a detailed assessment of the dynamic properties of the extended Gao beam model.

As a preliminary step, we refer to the comparison of Gao beam characteristic responses under Bernoulli-Euler and Timoshenko assumptions in dimensional form, as presented in [27]. This comparison illustrates the magnitude of the differences between the two theories, allowing for a clearer assessment of the influence of shear deformations. While a comprehensive study including engineering recommendations is beyond the scope of this work and will be addressed in a subsequent publication, several initial observations can be made. For an initial mid-point displacement of 0.2 cm and zero axial force, the Timoshenko-type model exhibits a slightly longer vibration period than the Bernoulli-Euler-type version, consistent with theoretical expectations. Under an axial force of $p = 575$ kN and damping, both models exhibit a characteristic nonlinear decay in vibration amplitude. The predicted equilibrium states differ; notably, the vibration amplitude of the thick model exceeds that of the thin model by more than 35% (Fig. 4). Given that both formulations are highly nonlinear, these comparisons remain primarily illustrative; a detailed quantitative study regarding the influence of specific material constants and loading conditions is the subject of ongoing research.

The present analysis covers the problems of free vibration (without axial compressive force), vibration under supercritical compressive force, and the dynamic response of the beam to an inertial moving load. In the engineering context, and particularly in the design of structural elements subject to dynamic and axial loading, it is essential to precisely determine the magnitude of the axial force relative to the cross-section dimensions that may occur in a given physical problem. This analysis allows for the quantification of the influence of the axial force on the magnification of internal forces and displacements compared to the estimations based on simplified, commonly used beam models (e.g., linear Timoshenko or Bernoulli-Euler models).

5.1. Numerical methods used

The choice of the integration method is crucial for the accuracy and stability of solving dynamic problems. For the nonlinear differential equations modelling the Gao beam, it is necessary to use a stable and sufficiently accurate scheme. The time integration of the equations of motion was performed using a space-time finite element approach [10,30,31]. This method was chosen for its conceptual clarity and the ease of physical interpretation of its results. Furthermore, in certain cases, it is computationally equivalent to the popular Newmark method [32] under optimal parameter selections that govern stability and damping. The numerical implementation was carried out in Fortran 95. Built-in matrix operations were utilised, which significantly streamlined the coding process. To solve the systems of algebraic equations in each time step, resulting from the space-time discretisation, the efficient Lapack DGBSV procedure [33] was employed. This procedure is optimised for working with banded coefficient matrices, which naturally arise from the local nature of finite elements, and saves computational resources. The solution of the equation in a single, nonlinear time step was obtained using Newton's method. Although the Newton-Raphson method was also tested, Newton's method was ultimately

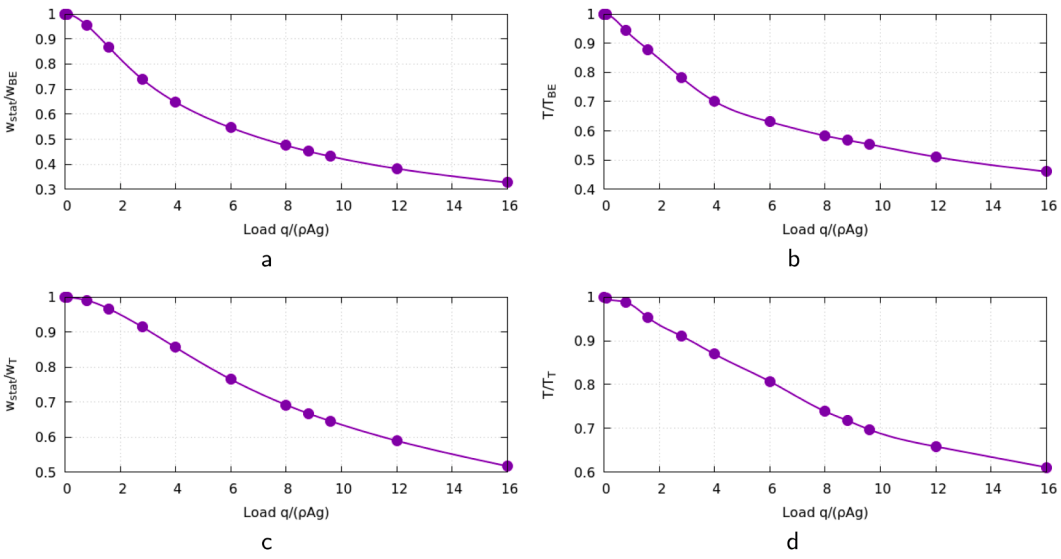

Fig. 5. Comparison of deflections w in mid-point and vibration period T for various load intensity in the case of thin Gao beam and thick Gao beam (with $p=0$): a– deflection of thin beam, b– period of thin beam, c– deflection of thick beam, d– period of thick beam.

adopted. This was due to the small time increment Δt used during integration and the resulting smoothness of the solutions. Given the small number of degrees of freedom and the narrow bandwidth of the system matrix, both methods achieved high accuracy for the trajectories within only a few iterations. The simpler-to-implement Newton's method proved to be sufficient in terms of computational effectiveness in this context.

5.2. *Free vibration without compression: assessment of model nonlinearity*

The purpose of the preliminary studies was to estimate the magnitude of the geometric nonlinearity introduced by the Gao model (both thin and thick) in the most basic case-free vibration. This is a crucial step before moving on to the analysis of complex dynamic interactions. To understand the fundamental properties of the model, the nature and magnitude of the geometric nonlinearity present in the thin Gao beam and thick Gao beam models (with zero compressive force $p=0$) were first investigated. The results were obtained from simulations of a simply supported beam ($L=100$ cm, 40 finite elements) subjected to a uniformly distributed load q. The applied uniformly distributed load facilitates a straightforward estimation of both the stiffness and the fundamental natural frequency across various ranges of nonlinearity. Zero initial conditions for both displacement and velocity were assumed. Since the axial force is $p=0$, the applied load q induces free vibrations around the zero equilibrium position. To determine subsequent points on the curves in Fig. 5, increasingly higher loads q were applied, resulting in a growing contribution of nonlinear terms. These, in turn, increased the beam's stiffness, consequently reducing deflection and shortening the vibration period compared to linear models. For both the thin and thick Gao beams, the results were referenced to the deflections (w_{BE}, w_{T}) and vibration periods (T_{BE}, T_{T}) obtained analytically using the linear Bernoulli-Euler and Timoshenko beam models, respectively. The deflection values w corresponding to the static equilibrium positions were determined from numerical simulations as half of the free vibration amplitudes. The vibration period T was determined from numerical simulations of free vibrations as the time interval between successive displacement peaks.

Fig. 5 illustrates the fundamental difference between the linear model and the Gao model. As the vibration amplitude caused by the load increases, the Gao beam model exhibits increasing stiffness (nonlinear geometric stiffening behavior effect). The normalised static deflections w_{stat} (representing flexibility/compliance) decrease. It should be emphasized that this stiffening effect is purely geometric in origin and results from nonlinear kinematic relations associated with large displacements, while the material model remains strictly elastic.

To facilitate the interpretation of the diagrams in Fig. 5, it can be noted that if the non-linear terms of the Gao beams were neglected, all points forming the curves in Fig. 5 would have ordinates equal to 1.0. Since these non-linear terms stiffen both beams, the points on the curves take on values less than 1 as the load q increases and stiffness increases. The static deflections w_{stat} can be treated as the beam's compliance at a given load level.

The increase in stiffness for deflections of the order of 1–2 cm ($w/L=0.01$–0.02) can reach a two- to threefold magnification compared to the linear Bernoulli-Euler model. The consequence of this is a dynamic effect in the form of a significant shortening of the vibration period T, which can be reduced by about half under high load (Fig. 5b, d). These results strongly indicate that neglecting nonlinearity in this range of deflections leads to large discrepancies with linear models in estimating vibration frequencies and periods.

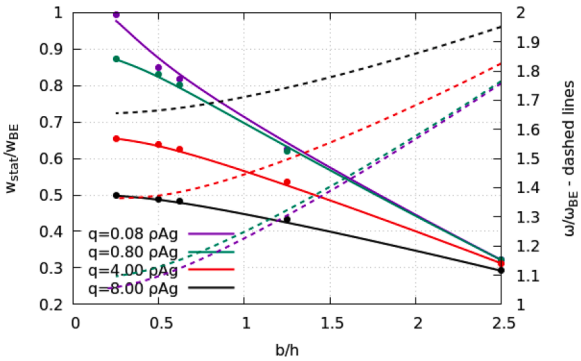

Fig. 6. Influence of the discretisation parameter b/h on the normalised static deflection w_{stat}/w_{BE} of the Gao beam (solid lines), where $w_{\mathrm{BE}} = 5qL^4/(384EI)$ is the Bernoulli-Euler deflection, and on the normalised first natural frequency ω/ω_{BE} in free vibration (dashed lines) related to the Bernoulli-Euler first natural frequency $\omega_{\mathrm{BE}} = (\pi^2/L^2)\sqrt{EI/(\rho A)}$.

5.3. Influence of numerical modelling error

Direct dynamic comparisons between the thin Gao beam model and the thick Gao beam model are subject to the non-uniformity of the numerical formulation. Higher-order approximations were used for the thin beam, while, to avoid excessive computational complexity, linear approximations were used for the thick beam in the context of the finite element method. This difference generates the known shear locking problem in the thick beam formulation. Although a detailed analysis of this phenomenon is beyond the scope of this work, it is necessary to present its key illustrations.

Fig. 6 shows the influence of discretisation parameters on the static stiffness of the model. It demonstrates that a fine discretisation, characterised by a low ratio of element length b to cross-sectional height h, yields an error on the order of 2–4%, compared with analytically obtained amplitude and natural frequency. The plot includes values obtained for five different b/h ratios. It should be noted that Fig. 6 illustrates the deflections of a Gao (Timoshenko-like) thick beam relative, for simplicity, to the deflections of a linear Bernoulli-Euler beam obtained analytically. Consequently, for a small load of $q = 0.08\rho Ag$ and a low b/h ratio, the data point on the graph even exceeds 1.0 (since the deflection of the Timoshenko beam in theory exceeds the deflection of the Bernoulli-Euler beam; for the applied data, the difference of both models is 1.6%).

In turn, when using a coarse discretisation (in Fig. 6, this refers to the value of $b/h = 2.5$), the over-stiffening of the structure under a small load is significant, and the resulting deflections represent approximately 35% of the exact value. For coarse discretisation (large b/h), the solution is affected by numerical artefacts, primarily shear locking associated with linear interpolation functions, leading to an overestimation of stiffness. As the element length b decreases, the numerical solution converges towards the analytical Timoshenko solution. This convergence trend becomes more pronounced for finer discretisations, confirming that the observed deviations for larger b/h are of numerical origin rather than a result of physical nonlinearity.

As a reference, the exact deflection and vibration period for the linear Timoshenko model were obtained analytically. These are denoted in the plots as w_{T}. In the Gao nonlinear model, under very low loading and the resulting small deflections, where the influence of nonlinear terms on the results is negligible, these values were taken as the exact solutions. In practice, the Timoshenko and Gao models coincide when nonlinear terms are neglected. In this case, points with a value of 1.0 were obtained in Fig. 5 for a load $q/(\rho Ag)$ close to 0. As the load increases, the nonlinear terms begin to exert a stronger influence on the results for the Gao beam, making it increasingly stiff. Consequently, the deflections decrease.

For the further presented simulations, a total of 100 elements were used with a ratio of $b/h = 0.12$. At this level of refinement, the quantitative numerical errors were considered negligible. Regarding the natural frequencies under low loading, the error decreases as b is reduced and the number of elements increases. In this case, the trend is represented by the purple dashed line.

It is observed that the nonlinear terms in the governing equation enhance the system stiffness as deflection increases. Furthermore, the results suggest that reducing the slenderness ratio (b/h) improves numerical accuracy. Specifically, under small loads and deformations, the values converge toward those obtained from linear Bernoulli-Euler or Timoshenko beam models.

5.4. Free vibration under compression

The introduction of an axial compressive force in nonlinear beam models leads to the phenomenon of static and dynamic bifurcation. This involves a jump change in the equilibrium position, which is a characteristic feature of nonlinear systems (snap-through phenomenon). Next, the free vibration of a thick beam (with an 8×8 cm cross-section, made of steel) compressed by a force p was investigated. The initial conditions were taken as the displacements corresponding to the static deflection under uniform load and zero initial velocity of the beam.

Fig. 7 illustrates this phenomenon, identifying the value $p = 6$ MN as the critical axial force ($p/p_b = 0.88$, p_b - buckling force). The time axis is scaled by the first natural frequency of the classical Timoshenko beam ω_{T}. Below this p value, the system oscillates

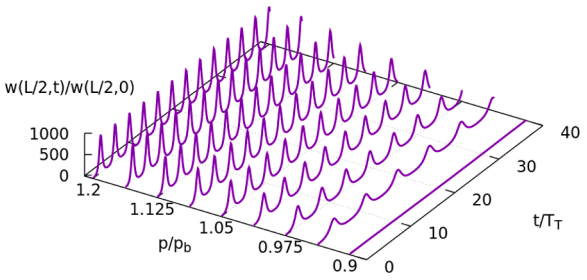

Fig. 7. Displacements of the mid-point of the thick Gao beam over time t at different values of the compressive axial force p (p_b - buckling force, T_T - fundamental period of the Timoshenko beam).

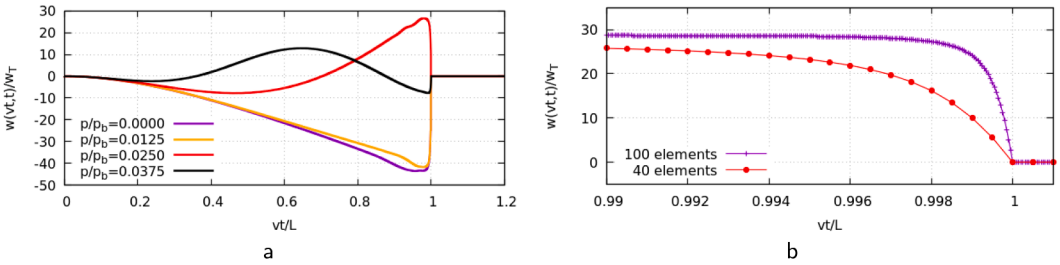

Fig. 8. Displacement in time of the follower point (a) and convergence to zero in last 1/100 of the span passage time with 40 and 100 spatial elements and condensed time step for $p/p_b = 0.025$ (b) (Deflection relative to the midpoint displacement of the Timoshenko beam w_T for a central point load mg; only every nth time step is depicted).

around the equilibrium position $w(x) = 0$. In contrast, above $p = 6$ MN, the oscillations occur around a non-zero equilibrium position ($w(x) > 0$ or $w(x) < 0$). This phase transition has been described in detail for the thin beam in [17] and for the thick beam in [27,28].

5.5. Discontinuity of the moving mass trajectory

The introduction of an inertial moving load induces wave phenomena in the beam. A characteristic feature for systems governed by hyperbolic equations (or wave equations) is the occurrence of kinematic discontinuities in the load contact regions. The phenomenon of discontinuity of the transverse displacement of the point tracking the load (moving mass) near the end support was investigated. This is a key feature of dynamic systems with a moving mass, proven for linear beams [9,11]. In the case of the nonlinear Gao model, this phenomenon is also observed.

In the numerical example, the following dimensionless parameters were adopted, consistent with the parameters used in [9]: $L = 1$, $A = 1$, $E = 1$, $I = 0.01$, $\upsilon = 0.5$, $m = 1$, $P_0 = mg = 1$. Fig. 8 illustrates this phenomenon. The displacement of the follower point, which increases under load, rapidly approaches zero in the last segment of the span just before leaving the support.

This phenomenon was first identified and demonstrated in string [11] and Timoshenko beam [9]. A rapid change in deflection at the tracking point, and the consequent increase in acceleration, is observed in practice. Railway catenary wires, unless specifically engineered for protection, tend to sustain damage at the ends of spans. Similarly, concrete slabs on expressways crack more frequently at the end of a load passage, specifically at the departure point. While this can be mathematically proven in models governed by equations with hyperbolic terms, models described only by parabolic terms (such as the Bernoulli-Euler beam) only demonstrate higher tracking point displacement values without trajectory discontinuities. It must be emphasised that this phenomenon is entirely due to the presence of the inertial term in the moving load; it does not occur in problems involving massless loads. The moving inertia effectively 'holds' the beam or slab at a level resulting from the transverse momentum imparted to the mass along the preceding sections of the span, where deflections are typically significant. The higher the velocity of the inertial load, the more difficult it becomes, due to the shorter timeframe, to reverse its transverse motion toward the support at the zero-equilibrium position.

The visibility and intensity of this discontinuity (manifesting in acceleration jumps) is strongly dependent on the problem parameters, especially the relationship between hyperbolic (Timoshenko) and parabolic, dispersive effects, described by a bi-harmonic equation (Bernoulli-Euler).

5.6. Multiple paths of the inertial load over the compressed span

This scenario combines three key elements: geometric nonlinearity, inertial (moving) load, and supercritical axial force (loss of stability). Such conditions are characteristic of railway bridges or viaduct structures with large thermal forces or pre-stresses. The following part provides a numerical analysis of the dynamic response of an elastic beam subjected to a cyclically moving mass (Fig. 9).

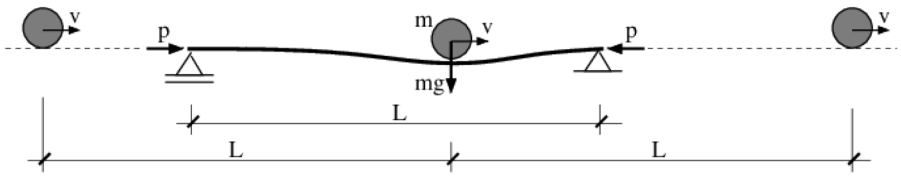

Fig. 9. Scheme of the beam under cyclic inertial moving load.

A steel beam with a length of $L=100$ cm and a square cross-section of 8×8 cm was subjected to a moving mass $m=5$ kg, generating a corresponding gravitational load. The axial compressive force p applied to the beam was 7 MN ($p/p_b=1.03$, p_b - buckling force). Fig. 10 illustrates the transverse displacements at the mid-span and at the load follower point for speeds $v=10$ m/s ($v/\sqrt{EI/(\rho A)}=0.08$), 30 m/s ($v/\sqrt{EI/(\rho A)}=0.25$), and 50 m/s ($v/\sqrt{EI/(\rho A)}=0.42$).

The beam length is L, but the mass passage is repeated. Consequently, the horizontal axis in Fig. 10 shows time scaled by the duration of a single traverse of the beam. The integers on the horizontal axis indicate the number of passes scaled by the time required to cover the length L (i.e., $1/(v/L)$). At the moment a mass exits the beam-which is already deformed and undergoing transverse motion-the next mass begins its traverse. Fig. 10 illustrates a fourfold passage.

Particular emphasis is placed on nonlinear effects resulting from the simultaneous action of a large compressive axial force and a small moving load, including the “snap-through” phenomenon. The influence of the mass transit speed on the beam’s displacements and accelerations was investigated to determine the nature of the system’s dynamic behaviour.

The combination of high axial compression and small transverse loading characterises the behaviour of diverse engineering systems. Practical examples include power line masts under self-weight and wind loading, as well as buried or subsea pipelines where thermal expansion induces high axial stresses. This loading condition is also prevalent in skyscraper columns supporting significant gravity loads and in rocket structures during the high-thrust ascent phase, where minor aerodynamic or control-induced lateral forces can trigger non-linear P-Delta effects.

Under the applied large axial force and small moving load, the middle segment of the beam undergoes “snap-through” transitions between two equilibrium configurations, namely between the maximum deflection values of +7 cm and −7 cm (7% of the length). This behaviour can be compared to the curve corresponding to $p=7$ MN ($p/p_b=1.03$) in Fig. 7. The follower point on the beam experiences displacements in a similar range, although the shape of its response curve shows some differences.

At low transit speeds, the response pattern observed in successive passages is repeatable (Fig. 10a, b). The beam’s mid-span deflects under the load in the direction of its movement, and after unloading, it oscillates in the opposite direction. The same effect is observed at the follower point under the moving mass. Immediately before the load leaves the span, the follower point experiences displacements opposite to the load direction. A moment later, the boundary conditions at the end support reduce the displacement to zero. This cycle repeats in subsequent passages. This effect becomes even more visible at slightly higher speeds (Fig. 10c, d). The follower point experiences larger positive displacements, reaching about 2.5 cm (2.5% of the length). Simultaneously, the number of oscillations during a single passage decreases. A further increase in transit speed increases the positive displacements of the follower point, accompanied by an earlier increase in positive values before the support. Meanwhile, the mid-span vibrations become detuned from the mass passage cycle $T_m = L/v$, showing a period shorter than $T_m<L/v$, and with further speed increase – a period longer than $T_m>L/v$. Fig. 10 shows only four passages, but these trends were observed during multiple repetitions. Higher transit speeds cause displacements that significantly deviate from periodic behaviour.

The nature of the dynamic response in this problem is sensitive to both the initial conditions and the model data themselves. The deflections of selected beam points and the tracking point during successive passes of the inertial load may differ significantly in consecutive travel cycles. At the same time, it should be emphasised that the qualitative character of the dynamic response is preserved. Sensitivity to initial conditions was partially investigated and described in [28]. That work used Poincaré maps to demonstrate which attractors the vibrations converge to depending on the initial conditions of the problem. Attention must also be paid to the response frequency, which differs from the excitation frequency of the subsequent passes (e.g., Fig. 10e).

Fig. 11 shows the displacements of the midpoint of a beam compressed by a force $p=7$ MN, with dimensions 8x8x100 cm, subjected to a moving inertial load of varying magnitude (mass values ranging from 5 kg to 200 kg were adopted, $m/(\rho AL) = 0.1 \ldots 4.0$, according to the scheme in Fig. 9). The supercritical axial force p plays a dominant role in the dynamic response. In the initial phase of the process, the displacements follow the direction of the load; however, the beam can also oscillate around the equilibrium position on the opposite side of the zero value. This occurs in the case of loads $m/(\rho AL)=1$ and 4. The jump to oscillations around the opposite equilibrium position occurs when the load is near the support and temporarily does not play a significant role in shaping the deflections. In this context, the direction of the beam’s momentum determines the equilibrium position, that is, on which side of the beam the subsequent oscillations will occur.

It is also instructive to display the accelerations at the midspan of the beam and at the tracking point (Fig. 12). It turns out that the largest accelerations occur neither when the load passes the midspan nor when it enters the support region. The peak acceleration values are, to a good approximation, insensitive to the traversal speed, whereas the number of acceleration peaks decreases with increasing speed. The interpretation is as follows: the number of displacement and acceleration peaks decreases as the transit speed increases, as the beam does not have sufficient time to react to the rapid appearance of the subsequent mass. In the plots, time is

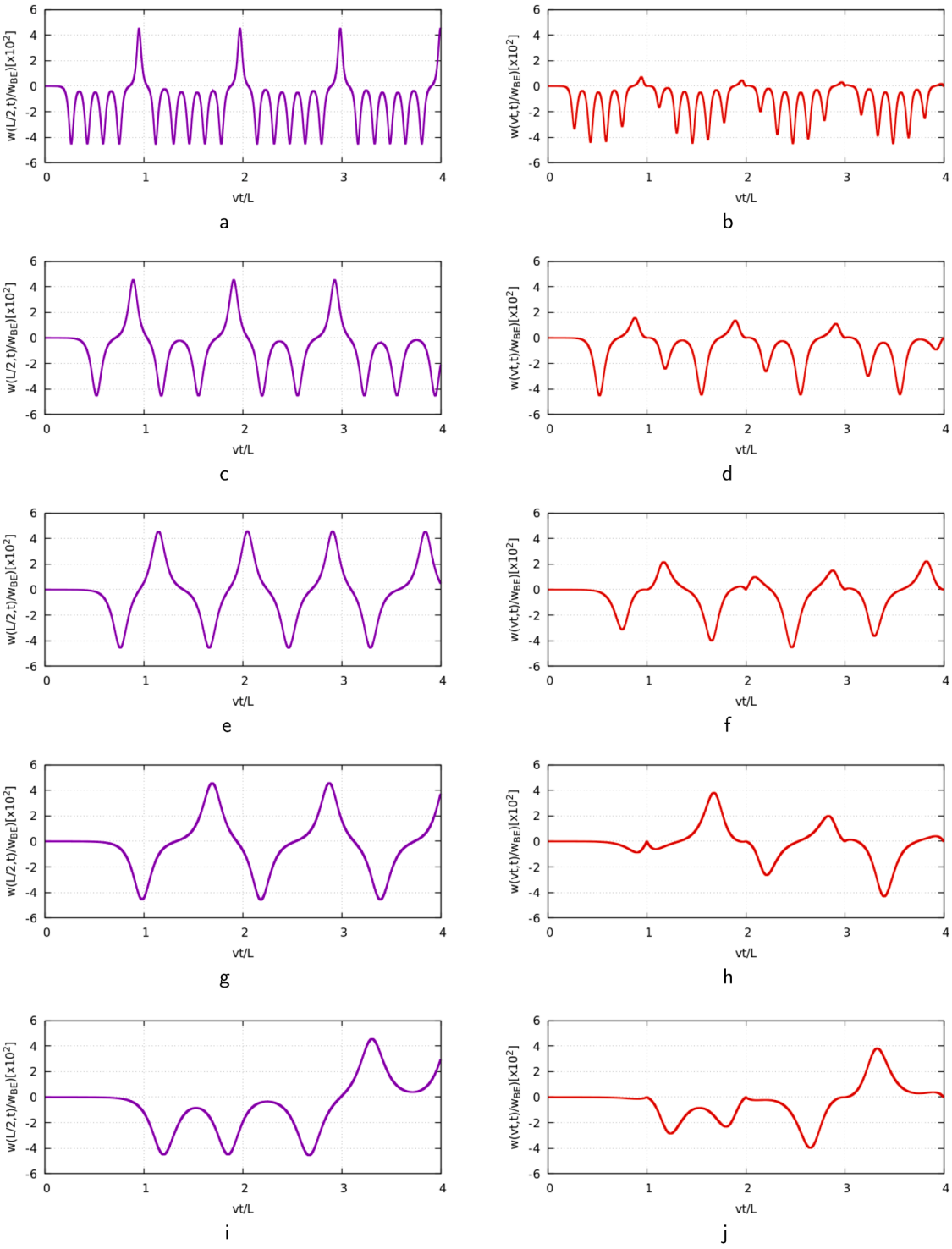

Fig. 10. Multiple path of the inertial point load in the mid-point and in the follower point, at a speed $v\sqrt{\rho A/(EI)}$: a, b- 0.08 (10 m/s), c, d- 0.17 (20 m/s), e, f- 0.25 (30 m/s), g, h- 0.33 (40 m/s), i, j- 0.42 (50 m/s); deflections related to the deflection of the Bernoulli-Euler beam under the point load mg in the mid-point $w_{\mathrm{BE}} = mgL^3/(48EI)$.

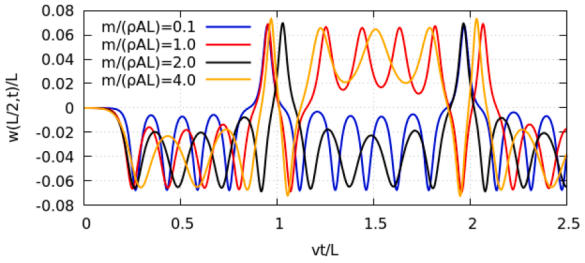

Fig. 11. Time-dependent displacements of the beam midpoint under a moving inertial load of varying magnitude.

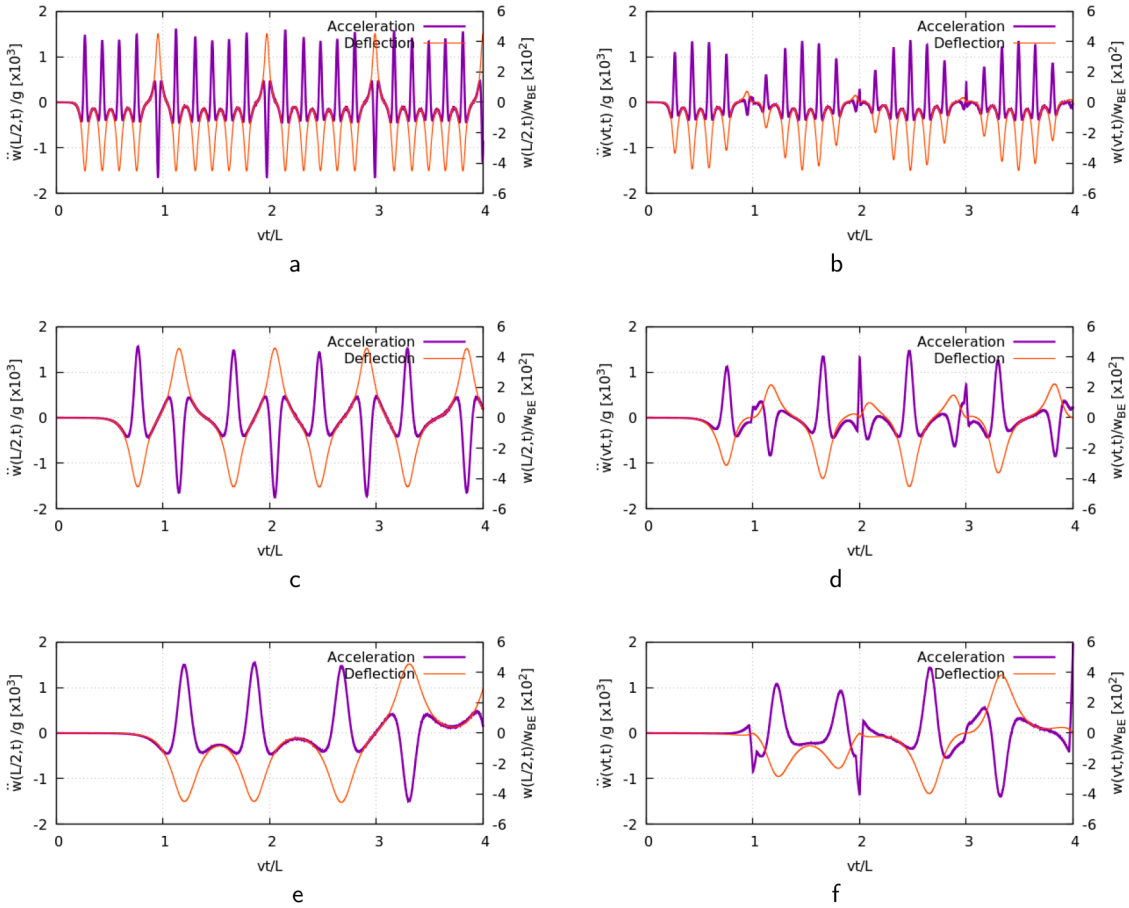

Fig. 12. Acceleration $\mathrm{d}^2w/\mathrm{d}t^2$ related to the acceleration of gravity g and deflection w related to the gravitational deflection in the midspan (a, c, e) and in the follower point (b, d, f) at the normalised speeds $v\sqrt{\rho A/(EI)}$ a, b- 0.08 (10 m/s), c, d- 0.25 (30 m/s), and e, f- 0.42 (50 m/s); deflections related to the deflection of the Bernoulli-Euler beam under the point load mg in the mid-point $w_{\mathrm{BE}} = mgL^3/(48EI)$.

scaled by the distance travelled. Real time elapses five times faster in Figures “e” and “f” than in Figures “a” and “b.” On the other hand, peak acceleration values remain unchanged during high-speed transit because the large displacements and accelerations are driven by the applied axial force, which is identical in all cases in Fig. 12. A similar interpretation applies to Fig. 11. This follows from the intrinsic dynamics of the beam itself, while the load acts primarily as an initiator of the vibrations. Nevertheless, it strongly affects the qualitative form of the response (Figs. 10 and 12). According to Fig. 7, as the force p decreases, the displacements and accelerations diminish. Upon dropping below the critical force of 6 MN ($p/p_b = 0.88$), the contribution of the moving load to the overall response increases. Consequently, vibrations occur about the equilibrium position $w(x,t) = 0$.

6. Conclusion and comments

The presented study on the mechanics of a compressed thick beam subjected to a moving inertial load provides key insights into the dynamics of this type of system. The most significant finding is that the deflections of the compressed beam are independent of the magnitude of the applied moving load, but are strongly modulated by the level of the axial compressive force.

Even a small load can regularly induce a deflection of the span in the opposite direction to the external force vector (a negative load causes upward displacement), which confirms the importance of the compressive force as the dominant parameter controlling the system's dynamics. It was observed that multiple passes of the same mass result in different response patterns, suggesting a high sensitivity to initial conditions or nonlinear dynamic interactions along the beam. Furthermore, when a downward-directed load induces deflection jumps above the zero line, the beam point subjected to a negative load exhibits significant positive displacements. Another crucial discovery is the strong detuning of deflection oscillations from the moving mass transition cycles. The analysis of accelerations at the beam's mid-span and the tracking point is also insightful. It reveals that the largest accelerations do not occur either when the mass passes the mid-span or when the load enters the support region. The peak acceleration values are, to a good approximation, insensitive to the speed of travel, while the number of acceleration peaks decreases with increasing speed. This phenomenon, along with the observation of a discontinuous mass trajectory, suggests complex resonances or instability phenomena that require further in-depth theoretical analysis. The potential applications of the presented model are broad, including: the design of vibro-isolation and vibration control systems (e.g., flow noise reduction in pipes), micro-electromechanical systems (MEMS) technology, and energy harvesting devices for capturing energy from motion. Of particular interest are the prospects for utilising these nonlinear interactions in flow control along flexible structures (beams/plates/pipes) and in protection against mechanical damage through effective energy dissipation. In light of these findings, further work is essential to establish comprehensive engineering guidelines. Future research should focus on accurately mapping the parameter space (compressive force, speed, and load mass) and on developing analytical models capable of predicting and controlling the described nonlinear dynamic responses.

CRediT authorship contribution statement

Bartłomiej Dyniewicz: Writing – original draft, Validation, Supervision, Software, Conceptualization; **Czesław I. Bajer:** Writing – review & editing, Visualization, Supervision, Software, Conceptualization; **Jitka Machalová:** Writing – original draft, Methodology, Formal analysis; **Horymír Netuka:** Writing – original draft, Methodology, Formal analysis.

Declaration of competing interest

The authors declare that they have no known competing financial interests or personal relationships that could have appeared to influence the work reported in this paper.

Acknowledgement

The authors gratefully acknowledge the support of the research by the following grant IGA_PrF_2025_015 Mathematical models.

Data availability

Data will be made available on request.

References

[1] L. Frýba, Vibrations of Solids and Structures Under Moving Loads, Thomas Telford House, 1999.
[2] G. Michaltsos, D. Sophianopoulos, A.N. Kounadis, The effect of a moving mass and other parameters on the dynamic response of a simply supported beam, J. Sound Vibr. 191 (1996) 357–362.
[3] J.E. Akin, M. Mofid, Numerical solution for response of beams with moving mass, J. Struct. Eng. 115 (1) (1989) 120–131.
[4] B. Biondi, G. Muscolino, A. Sidoti, Methods for calculating bending moment and shear force in the moving mass problem, J. Vib. Acoust. 126 (4) (2004) 542–552. https://doi.org/10.1115/1.1804992
[5] K. Kiani, A. Nikkhoo, B. Mehri, Parametric analyses of multispan viscoelastic shear deformable beams under excitation of a moving mass, J. Vib. Acoust. 131 (5) (2009) 051009. https://doi.org/10.1115/1.3147165
[6] A. Yavari, M.N. Mostafa, M. Mofid, Discrete element analysis of dynamic response of Timoshenko beams under moving mass, Adv. Eng. Softw. 33 (3) (2002) 143–153.
[7] P. Lou, G.-L. Dai, Q.Y. Zeng, Finite-element analysis for a Timoshenko beam subjected to a moving mass, Proc. Inst. Mech. Eng. C J. Mech. Eng. Sci. 220 (5) (2006) 669–678. https://doi.org/10.1243/09544062JMES119
[8] A. Ouzizi, F. Abdoun, L. Azrar, Nonlinear dynamics of Timoshenko beams on nonlinear fractional viscoelastic Pasternak foundation under a moving mass, Eng. Struct. 339 (2025) 120543. https://doi.org/10.1016/j.engstruct.2025.120543
[9] B. Dyniewicz, C.I. Bajer, New feature of the solution of a Timoshenko beam carrying the moving mass particle, Arch. Mech. 62 (5) (2010) 327–341.
[10] C.I. Bajer, B. Dyniewicz, Numerical Analysis of Vibrations of Structures Under Moving Inertial Load, Springer, 2012.
[11] B. Dyniewicz, C.I. Bajer, Paradox of the particle's trajectory moving on a string, Arch. Appl. Mech. 79 (3) (2009) 213–223.
[12] K.-Y. Lee, A.A. Renshaw, Solution of the moving mass problem using complex eigenfunction expansions, J. Appl. Mech. 67 (4) (2000) 823–827. https://doi.org/10.1115/1.1325010
[13] I. Esen, A new finite element for transverse vibration of rectangular thin plates under a moving mass, Finite Elem. Anal. Des. 66 (2013) 26–35. https://doi.org/10.1016/j.finel.2012.11.005
[14] B. Dyniewicz, D. Pisarski, C. Bajer, Vibrations of a Mindlin plate subjected to a pair of inertial loads moving in opposite directions, J. Sound Vib. 386 (2017) 265–282.

[15] E. Zupan, D. Zupan, Dynamic analysis of geometrically non-linear three-dimensional beams under moving mass, J. Sound Vib. 413 (2018) 354–367. https://doi.org/10.1016/j.jsv.2017.10.013
[16] C.I. Bajer, B. Dyniewicz, M. Shillor, A Gao beam subjected to a moving inertial point load, Math. Mech. Solids 23 (3) (2018) 461–472. https://doi.org/10.1177/1081286517718229
[17] B. Dyniewicz, C.I. Bajer, K.L. Kuttler, M. Shillor, Vibrations of a Gao beam subjected to a moving mass, Nonlinear Anal. Real World Appl. 50 (2019) 342–364. https://doi.org/10.1016/j.nonrwa.2019.05.007
[18] M.F. M'Bengue, Analysis of a Nonlinear Dynamic Beam with Material Damage or Contact, Ph.D. thesis, Oakland University, 2008.
[19] K.T. Andrews, Y. Dumont, M.F. M'Bemgue, J. Purcell, M. Shillor, Analysis and simulations of a nonlinear dynamic beam, Z. Angew. Math. Phys. 63 (6) (2012) 1005–1019. https://doi.org/10.1007/s00033-012-0233-9
[20] K.T. Andrews, K.L. Kuttler, M. Shillor, Dynamic Gao Beam in Contact with a Reactive or Rigid Foundation, Springer International Publishing, Cham, 2015, pp. 225–248. https://doi.org/10.1007/978-3-319-14490-0_9
[21] D.Y. Gao, J. Machalová, H. Netuka, Mixed finite element solutions to contact problems of nonlinear Gao beam on elastic foundation, Nonlinear Anal. Real World Appl. 22 (2015) 537–550. https://doi.org/10.1016/j.nonrwa.2014.09.012
[22] J. Machalová, H. Netuka, Control variational method approach to bending and contact problems for Gao beam, Appl. Math. 62 (6) (2017) 661–677. https://doi.org/10.21136/AM.2017.0168-17
[23] J. Radová, J. Machalová, J. Burkotová, Identification problem for nonlinear Gao beam, Mathematics 8 (11) (2022) 1–16. https://doi.org/10.3390/math8111916
[24] J. Radová, J. Machalová, Parameter identification in contact problems for Gao beam, Nonlinear Anal. Real World Appl. 77 (2022) 104068. https://doi.org/10.1016/j.nonrwa.2024.104068
[25] H. Netuka, J. Machalová, Post-buckling solutions for the Gao beam, Q. J. Mech. Appl. Math. 76 (3) (2023) 329–347. https://doi.org/10.1093/qjmam/hbad007
[26] D.Y. Gao, Nonlinear elastic beam theory with application in contact problems and variational approaches, Mech. Res. Commun. 23 (1) (1996) 11–17. https://doi.org/10.1016/0093-6413(95)00071-2
[27] B. Dyniewicz, M. Shillor, C.I. Bajer, An extended 2D Gao beam model, Meccanica 59 (2024) 169–181. https://doi.org/10.1007/s11012-023-01745-3
[28] B. Dyniewicz, M. Shillor, C.I. Bajer, Dynamic behavior of an extended Gao beam model including shear deformation, Nonlinear Anal. Real World Appl. 85 (2025) 104340. https://doi.org/10.1016/j.nonrwa.2025.104340
[29] A. Renaudot, Etude de l'influence des charges en mouvement sur la resistance, des ponts metallique a poutres droites, Ann. Ponts Chausses 1 (1861) 145–204.
[30] B. Dyniewicz, Space-time finite element approach to general description of a moving inertial load, Finite Elem. Anal. Des. 62 (2012) 8–17.
[31] C.I. Bajer, C. Bohatier, The soft way method and the velocity formulation, Comput. Struct. 55 (6) (1995) 1015–1025.
[32] N.M. Newmark, A method of computation for structural dynamics, ASCE J. Eng. Mech. Div. 85 (1959) 67–94.
[33] E. Anderson, Z. Bai, C. Bischof, L.S. Blackford, J. Demmel, J. Dongarra, J. Du Croz, A. Greenbaum, S. Hammarling, A. McKenney, D. Sorensen, LAPACK Users' Guide, Society for Industrial and Applied Mathematics, Philadelphia, PA, 3rd edition, 1999. https://doi.org/10.1137/1.9780898719604